

Quantum Coulomb drag signatures of Majorana bound states

Zi-Wei Li,¹ Jiaojiao Chen,¹ Wei Xiong,^{1,2,*} Xiao Xue,^{2,3} and Zeng-Zhao Li^{2,†}

¹*Department of Physics, Wenzhou University, Zhejiang, 325035, China*

²*International Quantum Academy, Shenzhen, 518048, China*

³*Hefei National Laboratory, University of Science and Technology of China, Hefei 230088, China*

(Dated: December 3, 2025)

Majorana bound states (MBSs), with their non-Abelian statistics and topological protection, are key candidates for fault-tolerant quantum computation. However, their unambiguous identification in solid-state systems remains a fundamental challenge. Here, we present a theoretical study demonstrating that drag transport in a capacatively coupled double quantum dot system offers a robust and nonlocal probe of weakly coupled MBSs. Using the master equation approach, we investigate both steady-state and transient dynamics and uncover a distinctive signature of MBSs, i.e., the emergence of pronounced split peaks in the drag transconductance, directly linked to inter-MBS coupling. We further show that the dynamics of quantum coherence exhibit an inverse correlation with the emergence and enhancement of MBS-induced split peaks in the drag transconductance as the inter-MBS coupling increases. A comparative analysis with Andreev bound states (ABSs) reveals key differences, that is, MBS-induced transconductance peaks are symmetric and robust, while ABS features are asymmetric and sensitive to perturbations. These findings establish clear experimental criteria for distinguishing MBSs and provide a practical framework for probing Majorana physics through nonlocal transport.

Majorana fermions, quasiparticles with non-Abelian statistics, are regarded as key building blocks for fault-tolerant topological quantum computation [1–14]. They are predicted to appear as Majorana bound states (MBSs) in topological superconductors, originally in spinless p -wave superconductors [15], and later in systems with spin-orbit coupling, external magnetic fields, and conventional s -wave superconductivity [16, 17]. Experimentally, a potential evidence of finding MBSs is the observation of zero-bias conductance peak [18, 19], which is a typical signature of MBSs. However, similar features can also be observed in the Andreev bound states (ABSs), leading to a great challenge in probing MBSs [20–29].

Recently, coupled double quantum dot (cDQD) systems have been proposed and rapidly emerged as promis-

ing candidates for probing MBSs [30–35]. cDQD not only allows precise control of charge and spin states, enabling high-fidelity detection, but also offers fine-tuning through gate voltages and magnetic fields [36]. Moreover, “poor man’s Majoranas” in cDQD have been demonstrated [37, 38], indicating that cDQD can offer an accessible, tunable, and scalable platform for studying MBSs’ behavior and non-Abelian statistics. Besides, the Coulomb drag effect [30–34] in cDQD, a current flow through a biased QD induces a measurable drag current in an unbiased QD, even in the absence of direct charge transfer, has proven to be a powerful probe for identifying MBSs from ABSs via studying steady-state drag current [35]. Although this method is promising, more definitive evidence and a deeper physical understanding of MBS signatures, particularly beyond conventional current measurements and steady-state transport, remain essential.

To this end, we present a theoretical study of quantum transport in a cDQD, where a biased QD is capacitively coupled to an unbiased dot connected to weakly hybridized MBSs. Within the master equation framework, we analyze both steady-state and transient dynamics. Our results reveal that, in addition to a pronounced drag current, a characteristic double-peak structure emerges in the transconductance, serving as a robust signature of nonlocal, Majorana-mediated transport. The time-resolved dynamics elucidate the emergence and stabilization of these signatures, clearly distinguishing them from transient non-Majorana effects. Furthermore, we study the dynamics of quantum coherence and find an inverse correlation between coherence and transconductance. Finally, we establish spectroscopic criteria for distinguishing MBSs from ABSs, based on transconductance peak symmetry and robustness against perturbations. These findings offer a practical framework for identifying MBSs and provide valuable insights for the design of topological quantum devices and non-equilibrium transport experiments in hybrid mesoscopic systems.

Results

The model and Hamiltonian

We consider a hybrid quantum system consisting of a cDQD with inter-dot capacitive interaction and a superconducting nanowire [Fig. 1(a)]. QD1 is driven by a bias voltage applied between two leads (i.e., the source lead S and the drain lead D), while QD2 is coupled to a normal lead N and to two spatially separated MBSs located

* xiongweiphys@wzu.edu.cn

† lizengzhao@iqasz.cn

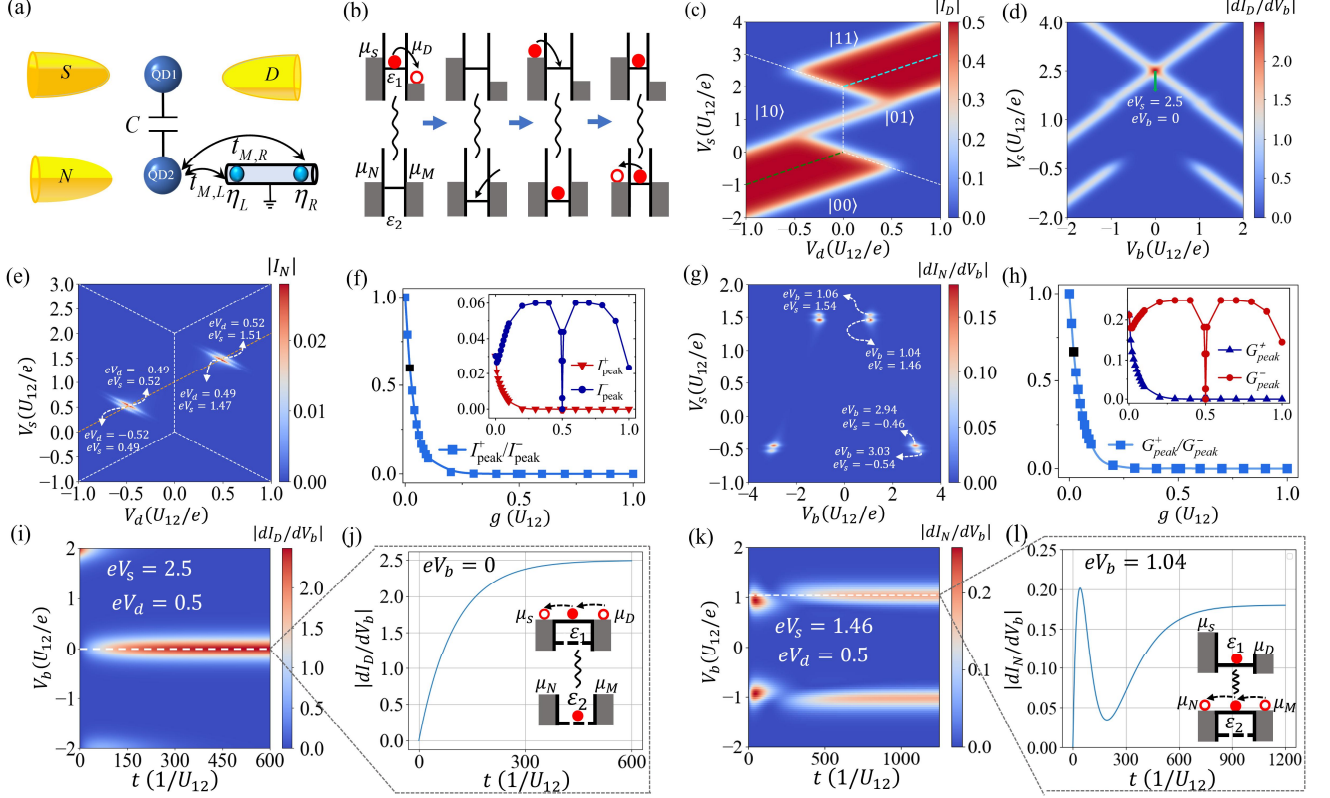


FIG. 1. Steady-state and transient transport signatures of MBSs. (a) Schematic illustration of the experimental setup for observing MBS-induced drag transport. A bias voltage applied across QD1 generates a drive current from source (S) to drain (D). Capacitive coupling between QD1 and QD2 induces a drag current through the unbiased QD2, which is connected to a normal metallic lead (N) and a proximitized Rashba nanowire hosting two weakly coupled MBSs, η_L and η_R , at its ends. The tunneling amplitudes between QD2 and the MBSs are denoted by $t_{M,L}$ and $t_{M,R}$. (b) Illustration of a representative sequence of tunneling events that drive the transition from the state $|10\rangle$ to $|11\rangle$, breaking the symmetry between forward and backward transport through QD2. (c) Drive current through QD1 as a function of gate voltages V_s and V_d under a fixed bias voltage $V_b = 1.04U_{12}$. (d) Differential conductance dI_D/dV_b at fixed $V_d = 0.5U_{12}$, showing a pronounced conductance peak at $(eV_b, eV_s) = (0, 2.5U_{12})$. (e) Drag current through QD2 as a function of V_s and V_d at $V_b = 1.04U_{12}$, revealing two symmetric pairs of MBS-induced current peaks. The upper and lower split peaks in one such pair near $eV_s = 1.5U_{12}$, located at $(eV_d, eV_s) = (0.52, 1.51)U_{12}$ and $(0.52, 1.49)U_{12}$, are labeled as I_{peak}^+ and I_{peak}^- , respectively. (f) Dependence of the peak current ratio $I_{\text{peak}}^+/I_{\text{peak}}^-$ on the inter-MBS coupling strength g , extracted from data in (e) with additional values of g [see Figs. S3(a)–S3(l) in Supplementary Sec. II B]. As $g \rightarrow 0$, the peak ratio approaches unity, indicating no observable splitting. The rapid suppression of I_{peak}^+ with increasing g leads to a sharp decline in the ratio. (g) Drag transconductance $|dI_N/dV_b|$ at fixed $eV_d = 0.5U_{12}$ showing four pairs of MBS-induced split peaks centered around $V_s = 1.5U_{12}$ and $V_s = -0.5U_{12}$. In the upper-right pair, the peaks located at $(eV_b, eV_s) = (1.06, 1.54)U_{12}$ and $(1.04, 1.46)U_{12}$ are denoted as G_{peak}^+ and G_{peak}^- , respectively. (h) The conductance peak ratio $G_{\text{peak}}^+/G_{\text{peak}}^-$ as a function of g , obtained from data in (g) with extended values of g [see Figs. S4(a)–S4(g) in Supplementary Sec. II C]. (i, k) Time evolution of the differential conductance of the drive current $|dI_D/dV_b|$ and the drag transconductance $|dI_N/dV_b|$ (in units of e^2), respectively, for $(eV_d, eV_s) = (0.5, 2.5)U_{12}$ and $(0.5, 1.46)U_{12}$. (j, l) Voltage slices of (i) and (k) taken at $eV_b = 0$ and $eV_b = 1.04U_{12}$, respectively. The long-time limits of (i) and (k) correspond to the steady-state points in (d) and (g) at $eV_s = 2.5U_{12}$ and $1.46U_{12}$, respectively. μ_M schematically represents the characteristic energy of the MBSs that serve as an effective bath for QD2. Other parameters are chosen as follows (in units of U_{12}): $\mu_S^{(0)} = \mu_D^{(0)} = \mu_N^{(0)} = 0$, $\Gamma_S = \Gamma_D = \Gamma_N = \Gamma_B = \Gamma_A = 0.01$, $k_B T = 0.05$, $g = 0.02$, and $\sigma = 0.01$. Drive and drag currents are given in units of $e\Gamma$, while differential conductances are expressed in units of e^2 . The cDQD system is initialized in the state $|\psi(0)\rangle = |00\rangle$.

at the ends of a superconducting nanowire with strong Rashba spin-orbit interaction. The Hamiltonian of the

proposed system can be written as (setting $\hbar = 1$)

$$H = H_{\text{cDQD}} + \sum_{\alpha} H_{\alpha} + H_{\text{MBS}} + H_T, \quad (1)$$

where $H_{\text{cDQD}} = \sum_j \varepsilon_j n_j + U_{12} n_1 n_2$ is the Hamiltonian

of cDQD, with $\varepsilon_j = -eV_j$ being the energy level of the j th QD (V_j is the gate voltage used to control the QD levels), and $U_{12} = e^2/2C$ (C is capacitive) the inter-dot capacitive coupling strength. The operator $n_j = d_j^\dagger d_j$ represents the occupation number of the j th QD, where d_j denotes the annihilation operator of the j th QD. The second term in Eq. (1), $H_\alpha = \sum_k (\varepsilon_{k,\alpha} - \mu_\alpha) c_{k,\alpha}^\dagger c_{k,\alpha}$ with $\alpha = S, D, N$, denotes the Hamiltonian of the lead α . The chemical potentials of the three leads are given by $\mu_S = \mu_S^{(0)} + eV_b/2$, $\mu_D = \mu_D^{(0)} - eV_b/2$, and $\mu_N = \mu_N^{(0)}$, where eV_b is the bias voltage applied to QD1, and $\mu_\alpha^{(0)}$ is the equilibrium chemical potential of lead α . $c_{k,\alpha}^\dagger$ ($c_{k,\alpha}$) is the creation (annihilation) operator of an electron in the lead α . The third term, $H_{\text{MBS}} = -ig\eta_L\eta_R$, represents the interaction between two separated MBSs with coupling strength g , where $\eta_{L(R)}$ denotes the Majorana mode at the left (right) end of the superconducting nanowire. The last term, H_T , characterizes the tunneling coupling between QD1 and the source and drain leads, and between QD2 and both the normal lead and the two spatially separated Majorana modes. In terms of a fermionic operator defined as $m = (\eta_L - i\eta_R)/\sqrt{2}$, H_T can be explicitly written as $H_T = (\sum_k t_{k,S} c_{k,S}^\dagger d_1 + \sum_k t_{k,D} c_{k,D}^\dagger d_1 + \sum_k t_{k,N} c_{k,N}^\dagger d_2 + \text{H.c.}) + t_A(m^\dagger d_2^\dagger + m d_2) + t_B(m^\dagger d_2 + m d_2^\dagger)$, where $t_{k,\alpha}$ is the tunneling amplitude between QD and the lead α , t_A is the coupling strength for simultaneous creation (annihilation) of an electron in QD2 and a complex fermion in the nanowire, and t_B is the coupling strength for conventional electron tunneling between QD2 and the fermionic mode. Specifically, $t_A = (t_{M,L} - it_{M,R})/\sqrt{2}$ and $t_B = (t_{M,L} + it_{M,R})/\sqrt{2}$, where $t_{M,L}$ ($t_{M,R}$) is the tunneling strength between QD2 and the left (right) MBS. As the Hamiltonian is expressed with the complex fermion m , the original Majorana operators $\eta_{L,R}$ no longer appear explicitly, and the Majorana character of the system is instead reflected in the symmetry and structure of the couplings.

With the basis spanned by the eigenstates of the isolated DQD, i.e., $\{|a\rangle = |00\rangle, |b\rangle = |10\rangle, |c\rangle = |01\rangle, |d\rangle = |11\rangle\}$, the total system Hamiltonian H in Eq. (1) can be rewritten as

$$\mathcal{H} = \mathcal{H}_{\text{cDQD}} + \sum_\alpha H_\alpha + H_{\text{MBS}} + H_T, \quad (2)$$

with

$$\begin{aligned} \mathcal{H}_{\text{cDQD}} &= \varepsilon_1|b\rangle\langle b| + \varepsilon_2|c\rangle\langle c| + (\varepsilon_1 + \varepsilon_2 + U_{12})|d\rangle\langle d|, \\ \mathcal{H}_T &= \sum_k \left[(t_{k,S} c_{k,S}^\dagger + t_{k,D} c_{k,D}^\dagger)(|a\rangle\langle b| + |c\rangle\langle d|) \right. \\ &\quad \left. + t_{k,N} c_{k,N}^\dagger (|a\rangle\langle c| - |b\rangle\langle d|) \right. \\ &\quad \left. + (t_A m^\dagger + t_B m)(|c\rangle\langle a| - |d\rangle\langle b|) \right] + \text{H.c.}, \end{aligned}$$

where H_α is the same as that defined in Eq. (1), and $H_{\text{MBS}} = gm^\dagger m$. The Hamiltonian in Eq. (2) captures the essential features of unidirectional electron transport

mediated by quantum tunneling, for example as illustrated in Fig. 1(b). Consider a representative transport cycle in which QD1 is initially occupied while QD2 is empty. Due to the inter-dot Coulomb interaction, this occupation electrostatically shifts the energy level of QD2 upward, thereby temporarily suppressing its occupancy. Once the electron in QD1 tunnels out to the drain D , the energy level of QD2 relaxes, allowing an electron to subsequently tunnel from the lead M into QD2, and then into the normal lead N . This process corresponds to the state transition $|b\rangle \rightarrow |d\rangle$, reflecting a directionally correlated sequence of tunneling events mediated by inter-dot Coulomb coupling. The resulting transport cycle breaks the forward-backward symmetry and induces nonreciprocal transport in the passive dot, emphasizing the intrinsically nonequilibrium nature of the system.

Steady-state transport signatures of MBSs

In this work, we use the master equation approach to simulate the dynamics of the proposed system (see Supplementary Sec. I for details). We here focus our interest on the steady-state behavior, i.e., $\partial\rho/\partial t = 0$. Solving it with the normalization condition $\sum_i \rho_{ii} = 1$, the occupation probabilities ρ_{ii} in cDQD are directly obtained. These probabilities enable the evaluation of both the drive and drag currents, along with their corresponding differential conductance. Figure 1(c) shows the absolute value of the drive current as a function of the gate voltages $V_s = V_2 + V_1$ and $V_d = V_2 - V_1$, under a fixed bias voltage $eV_b = 1.04U_{12}$. The influence of varying bias voltage on the drag current is analyzed in Supplementary Sec. II A. Along the lines $V_s = V_d$ (green) and $V_s = V_d + 2U_{12}/e$ (cyan), the drive current has a pronounced enhancement, indicating that the tunneling effect is dominant along these two lines. The corresponding differential conductance in Fig. 1(d) exhibits a prominent zero-bias peak, originating from inter-dot Coulomb interactions that enable electron tunneling from QD1 to the drain lead D even under energy detuning conditions (i.e., $\varepsilon_1/U_{12} = -1$).

The drag current shown in Fig. 1(e) exhibits a distinctive pattern, i.e., two symmetric pairs of split and asymmetric peaks aligned along the red dashed line $V_s = V_d + U_{12}/e$. This feature serves as a clear signature of two weakly coupled and spatially separated MBSs, consistent with recent findings reported in Ref. [35]. Although the specific parameter choices differ slightly, our results based on the Lindblad master equation are in good agreement with those obtained using the rate equation approach in Ref. [35], indicating that quantum coherence plays a limited role in determining the steady-state drag current. More importantly, we precisely identify the peak positions of the upper-right pair in Fig. 1(e), for example at $(eV_d, eV_s) = (0.52, 1.51)U_{12}$ and $(0.49, 1.47)U_{12}$, with corresponding peak currents denoted by I_{peak}^+ and I_{peak}^- , respectively. Their ratio $I_{\text{peak}}^+/I_{\text{peak}}^-$, extracted from Fig. 1(e) with additional values of g [see Figs. S3(a)-S3(l) in Supplementary Sec. II B], is plotted in Fig. 1(f).

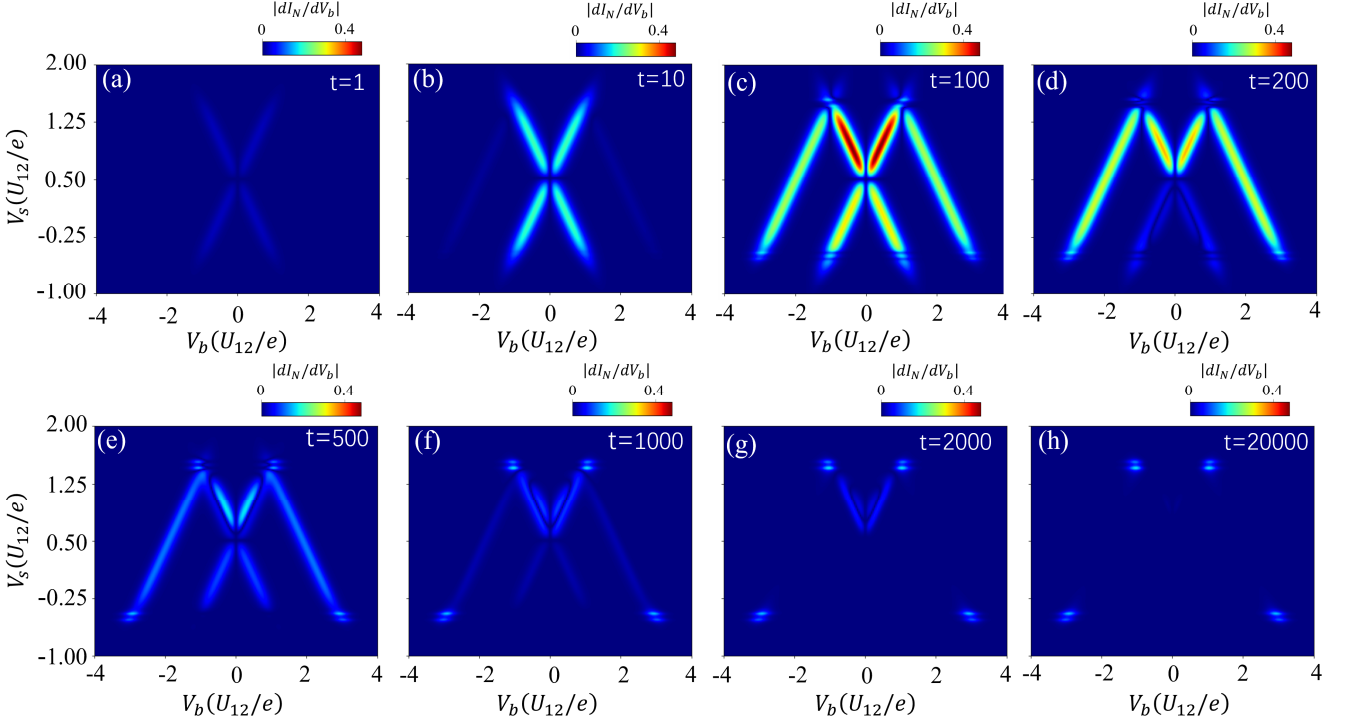


FIG. 2. The time-evolution characteristics of the drag conductance. Panels (a)–(h) depict the temporal evolution of differential drag conductance across the V_b – V_s parameter plane (t in units of $1/U_{12}$). Other parameters the same as those in Fig. 1 except for $eV_d = 0.5U_{12}$. The initial state for the time evolution is chosen as $|\psi(0)\rangle = |00\rangle$.

It exhibits a sharp decrease from near unity to nearly zero as the inter-MBS coupling g increases, primarily due to the suppression of I_{peak}^+ .

The drag transconductance in Fig. 1(g) displays four distinct pairs of peaks, with representative peak positions identified at, for example, $(eV_b/U_{12}, eV_s/U_{12}) = (1.04, 1.46)$ and $(1.06, 1.54)$, as well as $(2.94, -0.46)$ and $(3.03, -0.54)$ for $V_b > 0$. The observed peak splittings within each pair arise from finite hybridization between spatially separated MBSs, in contrast to the single peaks located at $(1.04, 1.50)$ and $(2.98, -0.50)$ that correspond to an isolated MBS coupled to QD2 [see Supplementary Sec. III A and III B for details]. As a specific example, the upper and lower peaks in the upper-right pair, denoted G_{peak}^+ and G_{peak}^- , exhibit a strongly asymmetric profile. The corresponding peak conductance ratio $G_{\text{peak}}^+/G_{\text{peak}}^-$, extracted from Fig. 1(g) for various values of g [see Figs. S4(a)–S4(g) in Supplementary Sec. II C], is plotted in Fig. 1(h), showing a sharp decline from 1 to 0 with increasing g . This behavior reflects the growing asymmetry in the transconductance profile driven by enhanced MBS hybridization. In the Supplementary, the steady-state transport in the case of two decoupled MBSs ($g = 0$) and a single isolated MBS are also given for comparison (see Fig. S9 in Sec. III C).

Transient transport signatures of MBSs

Next, we examine the transient dynamics to identify the

signatures of MBSs beyond the steady state. While the time evolution of the drive current is discussed in Supplementary Sec. II D, Fig. 1(i) shows the evolution of the differential conductance dI_D/dV_b at fixed gate voltages $eV_s = 2.5U_{12}$ and $eV_d = 0.5U_{12}$. A pronounced zero-bias conductance peak gradually develops and saturates around $t = 600$, consistent with the steady-state value observed at the same V_s in Fig. 1(d). This steady-state correspondence is further confirmed by the voltage slice at $eV_b = 0$ [indicated by the white dashed line in Fig. 1(i)], which is plotted in Fig. 1(j). Figure 1(k) presents the time evolution of the drag transconductance $|dI_N/dV_b|$ at $eV_s = 1.46U_{12}$ and $eV_d = 0.5U_{12}$, with the voltage slice at $eV_b = 1.04U_{12}$ shown in Fig. 1(l). The drag conductance displays nonmonotonic behavior, initially increasing, then decreasing, followed by a secondary rise before stabilizing at long times. This nonmonotonic dynamics results from the interplay between charge redistribution and capacitive coupling mediated by the MBSs under the bias applied to QD1. The corresponding transient dynamics of the drive and drag currents for these parameters is provided in Supplementary Sec. II E.

Dynamical emergence of MBSs

In addition to the pronounced peak splitting observed in the steady-state differential conductance [see Fig. 1(g)], a hallmark signature of inter-MBS coupling, we further examine the transient dynamics to elucidate the temporal evolution of MBS-mediated drag transport. Specif-

ically, we analyze the time-dependent behavior of the drag transconductance $|dI_N/dV_b|$ as a function of the normalized bias voltage $V_b/(U_{12}/e)$ and the symmetric gate voltage $V_s/(U_{12}/e)$, while keeping the antisymmetric gate voltage fixed at $V_d = 0.5U_{12}/e$. Figure 2 presents a sequence of temporal snapshots that trace the system's evolution from the initial nonequilibrium state to the emergence of a well-defined steady-state transport regime.

At the initial stage [Fig. 2(a)], the transconductance $|dI_N/dV_b|$ exhibits only weak and symmetric features around $V_b = 0$, indicating a minimal transient drag response. As time progresses to $t = 10$ [Fig. 2(b)], a distinct X-shaped pattern develops, reflecting the buildup of inter-dot correlations and the onset of nonlocal transport. With further evolution, the transconductance spectrum acquires a characteristic “M-shaped” profile in the V_b – V_s plane [Figs. 2(c)–2(f)]. Pronounced peaks emerge along $eV_s/U_{12} \approx -0.5$ and 1.5 , sharpening over time as resonant energy alignment is achieved between the QD₂ levels and the hybridized MBSs. During this intermediate stage ($100 \lesssim t \lesssim 1000$), signatures of Majorana modes become evident, marked by the emergence of non-local quantum correlations arising from coherent tunneling processes mediated by inter-dot Coulomb interactions and finite MBS hybridization. At later times [Figs. 2(g) and 2(h)], the transconductance amplitude gradually diminishes, signaling relaxation and equilibration toward a stationary regime. By $t = 20000$ (corresponding to 13.164 ns for $U_{12} = 1$ meV [32, 33]), the system reaches a steady state characterized by four pairs of asymmetric double peaks in the transconductance spectrum, closely matching the features in Fig. 1(g) (see Supplementary Sec. II F for the long-time transconductance distribution).

The observed time-resolved drag transconductance peaks originate from finite inter-Majorana hybridization, which lifts the degeneracy of the zero modes and signals the emergence of a nonlocal topological steady state. The peak spacing provides a direct dynamical measure of the coupling strength between the two MBSs, serving as a spectral fingerprint of spatially separated Majoranas and the nonlocal correlations they support. For comparison, the transient dynamics of the drag transconductance in the presence of a single isolated MBS are presented in Supplementary Sec. III D. Beyond their role as spectral markers, these time-resolved features offer experimentally accessible insight into the real-time evolution of Majorana physics, capturing the interplay between coherent tunneling and dissipative processes that govern drag transport in hybrid QD–MBS systems. These findings open new avenues for time-domain control and detection of Majorana-induced correlations in engineered quantum platforms.

Quantum coherence

Quantum coherence, a defining feature of quantum systems, plays a central role in quantum information processing and transport phenomena [39, 40]. It is character-

ized by the off-diagonal elements of the system's reduced density matrix, which reflect quantum superpositions. Our earlier findings reveal that, although coherence is present in the system, these off-diagonal terms do not directly contribute to steady-state transport quantities, such as the drive or drag currents and their corresponding conductances [see, e.g., Eqs. (7) and (8)]. In contrast, coherence plays a critical role in the transient regime, where it governs early-time charge dynamics, the emergence of drag currents, and the formation of nonlocal Majorana correlations. Time-resolved observables thus offer a valuable window into coherence effects that remain hidden in the steady state.

To explicitly investigate the dynamics of quantum coherence and their connection to Majorana signatures, we quantify the system's total coherence using the l_1 -norm measure [41], defined as

$$\mathcal{C}(t) = \sum_{i \neq j} |\rho_{ij}(t)|, \text{ with } i, j = a, b, c, d, \quad (3)$$

where $\rho_{ij}(t)$ are the elements of the reduced density matrix for cDQD, initialized in the coherent superposition state $|\psi(0)\rangle = \frac{1}{\sqrt{2}}(|b\rangle + |c\rangle)$. Meanwhile, we specifically examine the coherence characteristics characterized by the off-diagonal element ρ_{bc} , with detailed analysis provided in Supplementary Sec. IV. To assess the impact of inter-MBS coupling, we introduce the relative coherence,

$$c_{\text{rel}}(g, t) = \mathcal{C}(g, t)/\mathcal{C}(0, t) - 1, \quad (4)$$

where $\mathcal{C}(0, t)$ serves as the baseline coherence in the limit of negligible Majorana hybridization ($g \rightarrow 0$), corresponding to the case of a sufficiently long superconducting nanowire. Figures 3(a)–3(c) illustrate the evolution of relative quantum coherence c_{rel} as a function of time and bias voltage, highlighting the variation of coherence under different Majorana coupling strengths g , with respect to the uncoupled reference value. In Fig. 3(a) ($g = 0.02U_{12}$), a distinct coherence-enhancement region ($c_{\text{rel}} > 0$) emerges around $V_s \approx 1.5U_{12}/e$. As the coupling strength increases to $g = 0.06U_{12}$ and $0.1U_{12}$ [Figs. 3(b) and 3(c)], this enhanced region becomes more pronounced and expands, indicating that the Majorana coupling promotes coherence processes governed predominantly by the off-diagonal elements of the density matrix. Meanwhile, near the conductance-splitting region centered at $V_s \approx 1.5U_{12}/e$, a pair of symmetric grey regions appears, corresponding to areas with suppressed coherence ($c_{\text{rel}} < 0$). This suggests that, under certain gate-voltage conditions, the coupling to MBS can suppress quantum coherence. Notably, as g increases, the separation between these negatively correlated regions widens, reflecting an expanded range of Majorana-induced influence and a stronger modulation of the system's coherent dynamics.

To further examine this behavior, Figs. 3(d)–3(f) present the evolution of the absolute quantum coherence \mathcal{C} , which quantifies the total strength of the off-diagonal

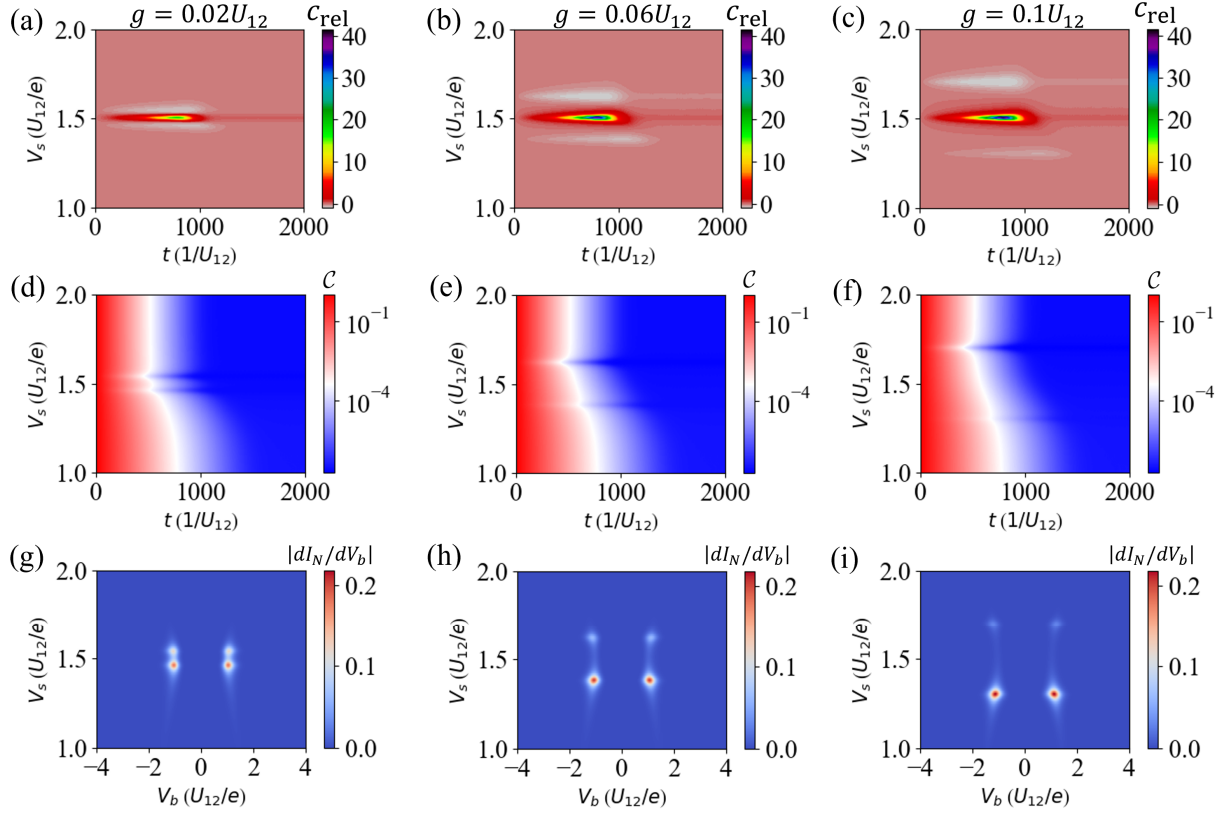


FIG. 3. Correlation between quantum coherence and conductance characteristics under different inter-MBS coupling strengths. Panels (a)–(c) show the evolution of the relative quantum coherence c_{rel} as a function of gate voltage V_s and time t , with (a) $g = 0.02U_{12}$, (b) $g = 0.06U_{12}$, and (c) $g = 0.1U_{12}$. Correspondingly, panels (d)–(f) present the evolution of the total off-diagonal coherence \mathcal{C} under the same coupling strengths. Panels (g)–(i) display the steady-state differential conductance $|dI_N/dV_b|$, highlighting its behavior near $V_s \approx 1.5U_{12}/e$. Other parameters are the same as those in Fig. 1 except for $V_d = 0.5U_{12}/e$. The initial state for the time evolution is chosen as $|\psi(0)\rangle = \frac{1}{\sqrt{2}}(|b\rangle + |c\rangle)$.

elements such as ρ_{bc} and ρ_{cb} . The coherence rapidly increases at early times and gradually decays due to dissipation caused by the leads. Two narrow features, where coherence sharply decreases to nearly zero, emerge and shift apart as g increases. This trend is consistent with the variation of c_{rel} , suggesting that under specific gate-voltage conditions, inter-Majorana coupling can destabilize the off-diagonal elements and suppress coherence.

Since g also affects the transport properties (the full influence of the inter-Majorana coupling strength g on conductance is detailed in Supplementary Sec. II C), Figs. 3(g)–3(i) displays the steady-state differential conductance $|dI_N/dV_b|$ under the same coupling strengths as in Figs. 3(a)–3(c). A conductance peak observed around $V_s \approx 1.5U_{12}/e$ [see Fig. S3(a) in Supplementary Sec. II C] gradually splits into two symmetric sub-peaks as g increases. This splitting indicates Majorana-induced level hybridization. Notably, the voltage region where this splitting occurs precisely corresponds to where the relative quantum coherence c_{rel} becomes negative, suggesting that although Majorana coupling enhances charge transport, it may simultaneously disrupt the internal coherent structure of the system, leading to localized suppression

of quantum coherence.

The study of quantum coherence here reveals a subtle and insightful phenomenon: the enhancement of quantum transport, such as conductance peaks, does not necessarily correlate positively with the evolution of coherence. Instead, distinct regions of conductance-coherence anti-correlation emerge. This observation is crucial for understanding the intricate relationship between transport signals and coherence preservation in topological quantum devices, and underscores the need to analyze conductance and coherence jointly to fully characterize the system's quantum dynamics.

Distinguishing Majorana Bound States from Andreev Bound States

A central challenge in tunneling experiments aimed at detecting MBSs lies in distinguishing them from near-zero-energy ABSs, which can also produce zero-bias conductance peaks [27, 28]. Physically, an ABS in a nanowire may be interpreted as a pair of spatially overlapping Majorana modes [26, 29]. Within the framework of cDQD, the effect of an ABS can be modeled using the same Hamiltonians H_α and H_T in Eq. (1), with one key modifi-

cation, e.g., the anomalous tunneling term vanishes (i.e., $t_A \approx 0$). Consequently, the quantum dot couples to the ABS solely via conventional electron tunneling,

$$H_T = t_B(m^\dagger d_2 + m d_2^\dagger),$$

with the ABS energy denoted by g , effectively taking the place of the inter-MBS coupling parameter in the MBS case.

For direct comparison, Fig. 4(a) shows the transconductance spectrum for MBSs along the orange dashed line ($V_s - V_d = 1$) in Fig. 1(e), while Figs. 4(b) and 4(c) display the corresponding results for an ABS-coupled system and a system with a single isolated MBS, respectively. A key distinguishing feature emerging in the ABS case is the drag transconductance peak near $eV_b/U_{12} = \pm 1$ remaining unsplit, in stark contrast to the characteristic peak splitting observed in the MBSs scenario. This absence of splitting provides a clear and reliable signature for differentiating ABSs from weakly coupled MBSs.

Additional insight arises from analyzing the peak symmetry. As illustrated in Fig. 4(b) and the orange solid curve in Fig. 4(d), ABS-induced peaks exhibit pronounced amplitude asymmetry, with the asymmetry directly originating from the intrinsic electron-hole imbalance of an ABS. In contrast, a Majorana mode possesses equal electron and hole spectral weights, enforcing a strictly symmetric conductance response under bias reversal. Accordingly, the conductance spectrum of an isolated MBS, shown in Fig. 4(c) and the blue dash-dotted curve in Fig. 4(d), lacks peak splitting but features a distinctly symmetric profile. Moreover, the transconductance features associated with coupled MBSs, shown in Fig. 4(d), remain symmetric and robust under variations in system parameters, consistent with their topological origin. This clear contrast in symmetry provides an additional spectroscopic criterion for experimentally distinguishing MBSs from ABSs.

It is important to highlight that, unlike the widely studied zero-bias tunneling conductance, our analysis focuses on the drag transconductance, where the current is measured through the unbiased QD2 while a bias voltage is applied only to the capacitively coupled QD1. This nonlocal configuration strongly suppresses trivial local backgrounds and makes the drag response particularly sensitive to Majorana-mediated processes. In this setting, a weakly coupled pair of MBSs produces a distinctive and robust peak splitting in the drag transconductance spectrum, a feature that is expected to persist under moderate perturbations due to the topological protection inherent to MBSs. By contrast, ABS-induced features might be less stable in this unbiased drag configuration. Their response is easily altered by Coulomb interactions or superconducting phase fluctuations, causing the associated peaks to shift. This sensitivity stands in sharp contrast to the robustness of the Majorana-induced splitting, making the unbiased transconductance a particularly clean and effective probe for distinguishing

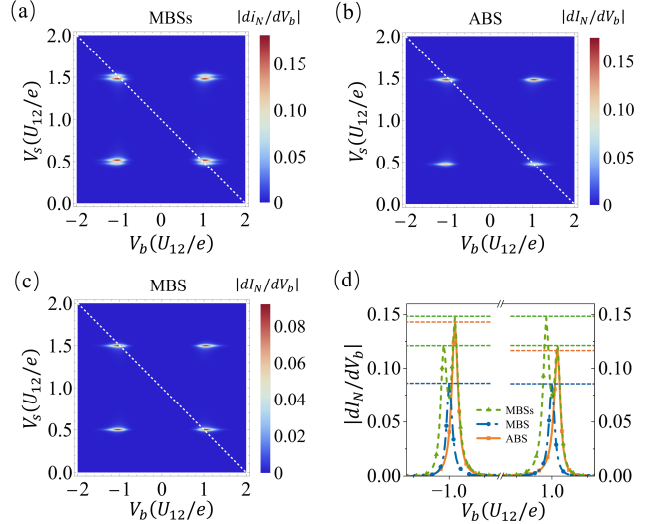


FIG. 4. Distinguishing MBSs from ABSs. Drag-current differential conductance versus V_b and V_s for (a) weakly coupled MBSs, (b) an ABS, and (c) an isolated MBS, taken along $V_s - V_d = 1$ [see the orange dashed line in Fig. 1(e)]. (d) Conductance profiles along the white dashed lines in (a)–(c) ($V_s = -V_b/2+1$) are compared for different states: two weakly coupled MBSs (green), an isolated MBS (blue), and a near-zero-energy ABS (orange). The inter-MBS coupling and ABS energy are set to $g = 0.02$ and other parameters are identical to those in Fig. 1.

MBSs from ABSs.

Conclusion and discussion

In summary, we theoretically investigate quantum transport in a cDQD system within a Markovian master equation framework. By analyzing the drag current and its differential transconductance, we identify unique signatures of inter-MBS coupling, particularly peak splitting phenomena that enable unambiguous differentiation from ABSs. Crucially, this splitting evolves dynamically over time, providing a robust time-resolved indicator of Majorana physics in the sequential tunneling regime. We further quantify relative quantum coherence via the ℓ_1 -norm, revealing an inverse correlation with conductance under varying inter-MBS coupling strengths. Comparative analysis between MBS- and ABS-coupled systems demonstrates fundamental distinctions: MBS-induced transconductance peaks exhibit symmetry and environmental robustness, whereas ABS-generated features display asymmetry and perturbation sensitivity. Together, these results establish a coherent framework for MBS detection and provide a route to design topological quantum devices based on MBSs.

Our analysis focuses on the sequential tunneling regime, where electron transport occurs through discrete tunneling events between QDs and leads. This approximation remains valid under weak QD-lead coupling and thermal energies exceeding tunneling rates, thereby suppressing higher-order processes like cotunneling [42–45].

Within this regime, the system dynamics are well captured by a Markovian master equation, which provides a tractable yet accurate framework for describing charge transport and quantum coherence. The Markovian approximation in fact assumes negligible memory effects due to clear timescale separation between system dynamics and environmental correlations. This allows for a simplified treatment of the dissipative evolution and tunneling processes. However, for a strong system-bath coupling or structured environments, non-Markovian effects may become important. In such cases, more general approaches, such as the Nakajima-Zwanzig formalism [46–48], could offer improved accuracy by explicitly incorporating memory effects. While our analysis remains within the Markovian regime, the methodology presented here lays a foundation for future extensions to non-Markovian dynamics under stronger coupling conditions.

The results presented in this work are experimentally feasible. Based on existing experiments (e.g., Ref. [32]), the differential conductance peaks corresponding to current magnitudes on the order of picoamperes (pA) are well within the detection capabilities of current nanowire-quantum dot platforms. Moreover, the conductance peak induced by MBSs reaches approximately $0.15 e^2$ (e.g., Fig. S6 in Supplementary Sec. II F), which exceeds the typical peak value of a single MBS, i.e., $\sim 0.08 e^2$ (Fig. S11 in Supplementary Sec. III D). Although ABSs can exhibit similar peak magnitudes, they feature pronounced asymmetries in both the height and position of the left and right peaks. Such asymmetric peak profiles serve as a distinguishing signature of ABSs relative to MBSs and are readily detectable using low-temperature lock-in techniques. Given that the MBS-induced conductance features are robust against small fluctuations in temperature and bias voltage, and that the required coupling strengths (such as U_{12} and the inter-MBS coupling g) have already been realized in InAs/Al nanowire experiments, the proposed drag conductance measurement

scheme is well within current experimental reach.

Our study goes beyond previous work such as Ref. [35], which focused exclusively on steady-state drag current, by systematically analyzing both the drag current and its differential transconductance, including their full time-dependent evolution. This broader perspective provides deeper insights into the dynamical behavior of Majorana-mediated transport and coherence in hybrid QD systems. Moreover, compared to the widely studied zero-bias conductance peak, which is often difficult to interpret due to its sensitivity to local disorder, gating fluctuations, and non-topological subgap states, our approach offers a conceptually distinct and experimentally robust alternative. In our setup, the quantum dot directly coupled to the MBSs is kept unbiased, thereby minimizing charge-fluctuation-induced disturbances and eliminating ambiguities associated with direct tunneling. Instead, a finite bias is applied only to a capacitively coupled auxiliary dot, which does not tunnel to the MBSs. This indirect-bias configuration enables nonlocal detection: Majorana signatures appear exclusively through the induced drag current and its transconductance. In particular, the emergence of well-resolved split peaks in the drag transconductance, arising from inter-MBS coupling, serves as a clear and experimentally accessible hallmark of Majorana physics. By avoiding direct perturbation of the MBS channel, this noninvasive scheme enhances robustness against local fluctuations and provides a promising pathway toward more conclusive identification of Majorana modes in mesoscopic systems.

Methods

We analyze quantum transport in cDQD within the framework of open quantum systems. By employing the master equation approach [49–51], the dynamics of the reduced density matrix ρ can be governed by (see Supplementary Sec. I for details)

$$\begin{aligned} \frac{\partial \rho}{\partial t} = & -i[\mathcal{H}_{\text{cDQD}}, \rho] \\ & + \frac{\Gamma_S}{2} \{ \bar{f}_S(\varepsilon_1) \mathcal{D}[|a\rangle\langle b|] \rho + f_S(\varepsilon_1) \mathcal{D}[|b\rangle\langle a|] \rho + \bar{f}_S(\varepsilon_1 + U_{12}) \mathcal{D}[|c\rangle\langle d|] \rho + f_S(\varepsilon_1 + U_{12}) \mathcal{D}[|d\rangle\langle c|] \rho \} \\ & + \frac{\Gamma_D}{2} \{ \bar{f}_D(\varepsilon_1) \mathcal{D}[|a\rangle\langle b|] \rho + f_D(\varepsilon_1) \mathcal{D}[|b\rangle\langle a|] \rho + \bar{f}_D(\varepsilon_1 + U_{12}) \mathcal{D}[|c\rangle\langle d|] \rho + f_D(\varepsilon_1 + U_{12}) \mathcal{D}[|d\rangle\langle c|] \rho \} \\ & + \frac{\Gamma_N}{2} \{ \bar{f}_N(\varepsilon_2) \mathcal{D}[|a\rangle\langle c|] \rho + f_N(\varepsilon_2) \mathcal{D}[|c\rangle\langle a|] \rho + \bar{f}_N(\varepsilon_2 + U_{12}) \mathcal{D}[|b\rangle\langle d|] \rho + f_N(\varepsilon_2 + U_{12}) \mathcal{D}[|d\rangle\langle b|] \rho \} \\ & + \frac{\Gamma_B}{2} \{ G_M(\varepsilon_2) [\bar{f}_M(\varepsilon_2) \mathcal{D}[|a\rangle\langle c|] \rho + f_M(\varepsilon_2) \mathcal{D}[|c\rangle\langle a|] \rho] \\ & \quad + G_M(\varepsilon_2 + U_{12}) [\bar{f}_M(\varepsilon_2 + U_{12}) \mathcal{D}[|b\rangle\langle d|] \rho + f_M(\varepsilon_2 + U_{12}) \mathcal{D}[|d\rangle\langle b|] \rho] \} \\ & + \frac{\Gamma_A}{2} \{ G_M(-\varepsilon_2) [\bar{f}_M(-\varepsilon_2) \mathcal{D}[|c\rangle\langle a|] \rho + f_M(-\varepsilon_2) \mathcal{D}[|a\rangle\langle c|] \rho] \\ & \quad + G_M(-\varepsilon_2 - U_{12}) [\bar{f}_M(-\varepsilon_2 - U_{12}) \mathcal{D}[|d\rangle\langle b|] \rho + f_M(-\varepsilon_2 - U_{12}) \mathcal{D}[|b\rangle\langle d|] \rho] \}, \end{aligned} \quad (5)$$

where $\mathcal{D}[\Lambda]\rho = 2\Lambda\rho\Lambda^\dagger - \rho\Lambda^\dagger\Lambda - \Lambda^\dagger\Lambda\rho$ is the Lindblad superoperator, $f_\alpha(\omega) = [1 + \exp((\omega - \mu_\alpha)/k_B T)]^{-1}$ and $f_M(\omega) = [1 + \exp(\omega/k_B T)]^{-1}$ are the Fermi-Dirac distributions for lead α and MBSs, respectively. The tunneling rate is given by $\Gamma_\alpha = 2\pi G_\alpha |t_\alpha|^2$, with G_α denoting the density of states of lead α . The effective couplings between QD2 and MBSs are $\Gamma_{A(B)} = 2\pi |t_{A(B)}|^2$. For convenience, we introduce $\bar{f}_{\alpha(M)} = 1 - f_{\alpha(M)}$. In our calculation, we model the density of states of MBSs using a Lorentzian distribution [35, 52],

$$G_M(\omega) = \frac{\sigma^2}{(\omega - g)^2 + \sigma^2}, \quad (6)$$

where σ denotes the broadening parameter and g is the inter-MBS coupling strength.

Using the elements ρ_{ij} of the reduced density matrix ρ in Eq. (5), the drive current flowing into the drain lead through QD1 is given by [53, 54]

$$I_D = e\Gamma_D [\rho_{bb}\bar{f}_D(\varepsilon_1) + \rho_{dd}\bar{f}_D(\varepsilon_1 + U_{12})] - e\Gamma_D [\rho_{aa}f_D(\varepsilon_1) + \rho_{cc}f_D(\varepsilon_1 + U_{12})], \quad (7)$$

while the drag current flowing into the normal lead through QD2 is

$$I_N = e\Gamma_N [\rho_{cc}\bar{f}_N(\varepsilon_2) + \rho_{dd}\bar{f}_N(\varepsilon_2 + U_{12})] - e\Gamma_N [\rho_{aa}f_N(\varepsilon_2) + \rho_{bb}f_N(\varepsilon_2 + U_{12})]. \quad (8)$$

To characterize transport response, we calculate the differential conductance dI_D/dV_b and dI_N/dV_b as functions

of the applied bias V_b . These quantities measure how sensitively the drive and drag currents respond to voltage modulation and serve as key diagnostics for identifying the underlying transport mechanisms.

For numerical calculations, we adopt the inter-dot Coulomb interaction U_{12} as the energy unit. We consider a symmetric lead configuration with chemical potentials $\mu_S = \mu_S^{(0)} + eV_b/2$, $\mu_D = \mu_D^{(0)} - eV_b/2$ and symmetric coupling strengths $\Gamma_S = \Gamma_D$. The system is assumed to be in the weak-coupling, low-temperature regime where $\Gamma_\alpha \ll k_B T \ll U_{12}$.

Acknowledgements

This work was supported by the Natural Science Foundation of Zhejiang Province (Grant No. LY24A040004), Zhejiang Province Key R&D Program of China (Grant No. 2025C01028), and Shenzhen International Quantum Academy (Grant No. SIQA2024KFKT010).

Author contributions

Z.W.L. performed the calculation. Z.W.L., J.C., W.X., X. Xue, and Z.Z.L. wrote the manuscript. Z.Z.L. and W.X. supervised the project.

Competing interests

The authors declare no competing interests.

Data availability

The datasets used to generate the plots in the paper are available on Zenodo. All other data that support the plots within this paper and other findings of this study are available from the corresponding authors upon reasonable request.

-
- [1] C. Nayak, S. H. Simon, A. Stern, M. Freedman, and S. D. Sarma, Non-Abelian anyons and topological quantum computation, *Rev. Mod. Phys.* **80**, 1083 (2008).
- [2] F. Wilczek, Majorana returns, *Nat. Phys.* **5**, 614 (2009).
- [3] A. Stern, Non-Abelian states of matter, *Nature* **464**, 187 (2010).
- [4] M. Leijnse and K. Flensberg, Introduction to topological superconductivity and Majorana fermions, *Semicond. Sci. Technol.* **27**, 124003 (2012).
- [5] J. Alicea, New directions in the pursuit of Majorana fermions in solid state systems, *Rep. Prog. Phys.* **75**, 076501 (2012).
- [6] C. W. J. Beenakker, Search for Majorana fermions in superconductors, *Annu. Rev. Cond. Mat. Phys.* **4**, 113 (2013).
- [7] S. D. Sarma, M. Freedman, and C. Nayak, Majorana zero modes and topological quantum computation, *npj Quantum Inf* **1**, 15001 (2015).
- [8] S. R. Elliott and Marcel Franz, Colloquium: Majorana fermions in nuclear, particle, and solid-state physics, *Rev. Mod. Phys.* **87**, 137 (2015).
- [9] R. Aguado, Majorana quasiparticles in condensed matter, *Riv. Nuovo Cimento* **40**, 523 (2017).
- [10] M. Sato and Y. Ando, Topological superconductors: A review, *Rep. Prog. Phys.* **80**, 076501 (2017).
- [11] R. Aguado and L. P. Kouwenhoven, Majorana qubits for topological quantum computing, *Phys. Today* **73**, 44 (2020).
- [12] K. Flensberg, F. von Oppen, and A. Stern, Engineered platforms for topological superconductivity and Majorana zero modes, *Nat. Rev. Mater.* **6**, 944 (2021).
- [13] Y. Tanaka, S. Tamura, and J. Cayao, Theory of Majorana zero modes in unconventional superconductors, *Prog. Theor. Exp. Phys.* **2024**, 08C105 (2024).
- [14] D. A. Ivanov, Non-Abelian statistics of half-quantum vortices in p-wave superconductors, *Phys. Rev. Lett.* **86**, 268 (2001).
- [15] A. Kitaev, Fault-tolerant quantum computation by anyons, *Ann. Phys.* **303**, 2 (2003).
- [16] R. M. Lutchyn, J. D. Sau, and S. Das Sarma, Majorana fermions and a topological phase transition in semiconductor-superconductor heterostructures, *Phys. Rev. Lett.* **105**, 077001 (2010).
- [17] Y. Oreg, G. Refael, and F. von Oppen, Helical Liquids and Majorana Bound States in Quantum Wires, *Phys. Rev. Lett.* **105**, 177002 (2010).

- [18] S. Nadj-Perge, I. K. Drozdov, J. Li, H. Chen, S. Jeon, J. Seo, A. H. MacDonald, B. A. Bernevig, and A. Yazdani, Observation of Majorana fermions in ferromagnetic atomic chains on a superconductor, *Science* **346**, 602 (2014).
- [19] J.-P. Xu, M.-X. Wang, Z. L. Liu, J.-F. Ge, X. Yang, C. Liu, Z. A. Xu, D. Guan, C. L. Gao, D. Qian, Y. Liu, Q.-H. Wang, F.-C. Zhang, Q.-K. Xue, and J.-F. Jia, Experimental detection of a Majorana mode in the core of a magnetic vortex inside a topological insulator-superconductor $\text{Bi}_2\text{Te}_3/\text{NbSe}_2$ heterostructure, *Phys. Rev. Lett.* **114**, 017001 (2015).
- [20] E. Prada, P. San-Jose, M. W. A. de Moor, A. Geresdi, E. J. H. Lee, J. Klinovaja, D. Loss, J. Nygård, R. Aguado, and Leo P. Kouwenhoven, From Andreev to Majorana bound states in hybrid superconductor–semiconductor nanowires, *Nat. Rev. Phys.* **2**, 575 (2020).
- [21] A. D. K. Finck, D. J. Van Harlingen, P. K. Mohseni, K. Jung, and X. Li, Anomalous modulation of a zero-bias peak in a hybrid nanowire-superconductor device, *Phys. Rev. Lett.* **110**, 126406 (2013).
- [22] C.-X. Liu, J. D. Sau, T. D. Stanescu, and S. Das Sarma, Andreev bound states versus Majorana bound states in quantum dot-nanowire-superconductor hybrid structures: Trivial versus topological zero-bias conductance peaks, *Phys. Rev. B* **96**, 075161 (2017).
- [23] K. Yavilberg, E. Ginossar, and E. Grosfeld, Differentiating Majorana from Andreev bound states in a superconducting circuit, *Phys. Rev. B* **100**, 241408(R) (2019).
- [24] C.-X. Liu, J. D. Sau, and S. Das Sarma, Topological Andreev bound states in quasi-Majorana wires, *Phys. Rev. B* **99**, 245306 (2019).
- [25] K. T. Law, Patrick A. Lee, and T. K. Ng, Majorana fermion induced resonant Andreev reflection, *Phys. Rev. Lett.* **103**, 237001 (2009).
- [26] C. Moore, T. D. Stanescu, and S. Tewari, Two-terminal charge tunneling: Disentangling Majorana zero modes from partially separated Andreev bound states in semiconductor-superconductor heterostructures, *Phys. Rev. B* **97**, 165302 (2018).
- [27] C. Moore, C. Zeng, T. D. Stanescu, and S. Tewari, Quantized zero-bias conductance plateau in semiconductor-superconductor heterostructures without topological Majorana zero modes, *Phys. Rev. B* **98**, 155314 (2018).
- [28] P. Yu, J. Chen, M. Gomanko, G. Badawy, E. P. A. M. Bakkers, K. Zuo, V. Mourik, and S. M. Frolov, Non-Majorana states yield nearly quantized conductance in proximatized nanowires, *Nat. Phys.* **17**, 482 (2021).
- [29] G. Kells, D. Meidan, and P. W. Brouwer, Near-zero-energy end states in topologically trivial spin-orbit coupled superconducting nanowires with a smooth confinement, *Phys. Rev. B* **86**, 100503(R) (2012).
- [30] R. Sanchez, R. Lopez, D. Sanchez, and M. Buttiker, Mesoscopic Coulomb Drag, Broken Detailed Balance, and Fluctuation Relations, *Phys. Rev. Lett.* **104**, 076801 (2010).
- [31] K. Kaasbjerg and A.-P. Jauho, Correlated Coulomb Drag in Capacitively Coupled Quantum-Dot Structures, *Phys. Rev. Lett.* **116**, 196801 (2016).
- [32] A. J. Keller, J. S. Lim, D. Sanchez, R. Lopez, S. Amasha, J. A. Katine, H. Shtrikman, and D. Goldhaber-Gordon, Cotunneling Drag Effect in Coulomb-Coupled Quantum Dots, *Phys. Rev. Lett.* **117**, 066602 (2016).
- [33] M. A. Sierra, D. Sanchez, K. Kaasbjerg, and A.-P. Jauho, Fluctuation-driven Coulomb drag in interacting quantum dot systems, *Phys. Rev. B* **100**, 081404 (2019).
- [34] S. M. Tabatabaei, D. Sanchez, A. L. Yeyati, and R. Sanchez, Andreev-Coulomb Drag in Coupled Quantum Dots, *Phys. Rev. Lett.* **125**, 247701 (2020).
- [35] X. Xiao and J. X. Zhu, Majorana bound state induced drag current in capacitively coupled quantum dots, *arXiv:2402.11730v1*.
- [36] Tom Dvir, Guanzhong Wang, Nick van Loo, Chun-Xiao Liu, Grzegorz P. Mazur, Alberto Bordin, Sebastiaan L. D. ten Haaf, Ji-Yin Wang, David van Driel, Francesco Zatelli, Xiang Li, Filip K. Malinowski, Sasa Gazibegovic, Ghada Badawy, Erik P. A. M. Bakkers, Michael Wimmer and Leo P. Kouwenhoven, Realization of a minimal Kitaev chain in coupled quantum dots, *Nature* **614**, 445 (2023).
- [37] M. Leijnse and K. Flensberg Parity qubits and poor man’s Majorana bound states in double quantum dots, *Phys. Rev. B* **86**, 134528 (2012).
- [38] S. L. D. ten Haaf, Q. Wang, A. M. Bozkurt, C.-X. Liu, I. Kulesh, P. Kim, D. Xiao, C. Thomas, M. J. Manfra, T. Dvir, M. Wimmer, and S. Goswami, A two-site Kitaev chain in a two-dimensional electron gas, *Nature* **630**, 329 (2024).
- [39] A. Streltsov, G. Adesso, and M. B. Plenio, *Colloquium: Quantum coherence as a resource*, *Rev. Mod. Phys.* **89**, 041003 (2017).
- [40] T. Baumgratz, M. Cramer, and M. B. Plenio, *Quantifying coherence*, *Phys. Rev. Lett.* **113**, 140401 (2014).
- [41] M. B. Plenio and S. Virmani, *An introduction to entanglement measures*, *Quantum Inf. Comput.* **7**, 1 (2007).
- [42] V. N. Golovach and D. Loss, Transport through a double quantum dot in the sequential tunneling and cotunneling regimes, *Phys. Rev. B* **69**, 245327 (2004).
- [43] J. Picó-Cortés, G. Platero, A. Donarini, and M. Grifoni, Nonequilibrium cotunneling in quantum dot Josephson junctions, *Phys. Rev. B* **110**, 125418 (2024).
- [44] S. L. Rudge and D. S. Kosov, Distribution of waiting times between electron cotunneling events, *Phys. Rev. B* **98**, 245402 (2018).
- [45] H. D. Cornean and V. Moldoveanu, On the cotunneling regime of interacting quantum dots, *J. Phys. A: Math. Theor.* **44**, 305002 (2011).
- [46] S. Nakajima, On quantum theory of transport phenomena: Steady diffusion, *Prog. Theor. Phys.* **20**, 948 (1958).
- [47] R. Zwanzig, Ensemble method in the theory of irreversibility, *J. Chem. Phys.* **33**, 1338 (1960).
- [48] Z. Z. Li, C. T. Yip, H. Y. Deng, M. Chen, T. Yu, J. Q. You, and C. H. Lam, Approach to solving spin-boson dynamics via non-Markovian quantum trajectories, *Phys. Rev. A* **90**, 022122 (2014).
- [49] V. Gorini, A. Kossakowski, and E. C. G. Sudarshan, Completely positive dynamical semigroups of N-level systems, *J. Math. Phys.* **17**, 821 (1976).
- [50] G. Lindblad, On the generators of quantum dynamical semigroups, *Commun. Math. Phys.* **48**, 119–130 (1976).
- [51] H. P. Breuer and F. Petruccione, *The Theory of Open Quantum Systems*, (Oxford University Press, New York, 2007).
- [52] M. Gibertini, F. Taddei, M. Polini and R. Fazio, Majorana bound states in interacting multi-band nanowires, *Phys. Rev. B* **85**, 144525 (2012).
- [53] R. A. Bush, E. D. Ochoa, and J. K. Perron, Transport through quantum dots: An introduction via master equa-

- tion simulations, [Am. J. Phys. **89**, 300 \(2021\)](#).
- [54] U. Harbola, M. Esposito, and S. Mukamel, Quantum master equation for electron transport through quantum dots and single molecules, [Phys. Rev. B **74**, 235309 \(2006\)](#).